Hybrid White Light Emitting Diode Based on Silicon Nanocrystals

*Batu Ghosh, Yoshitake Masuda, Yutaka Wakayama, Yasutaka Imanaka, Jun-ichi Inoue, Kenjiro Hashi, Kenzo Deguchi, Hideto Yamada, Yoshio Sakka, Shinobu Ohki, Tadashi Shimizu, and Naoto Shirahata**

A novel design of white light emitting diodes (WLEDs) emerges to meet the growing global demand for resource sustainability while preserving health and environment. To achieve this goal, a facile method is developed for the chemical synthesis of a luminescent silicon nanocrystal (ncSi) with a large Stokes shift between absorption and emission. The WLED is prepared by a simple spin-coating method, and contains a hybrid-bilayer of the ncSi and luminescent polymer in its device active region. Interestingly, a well-controlled ultrathin ncSi layer on the polymer makes possible to recombine electrons and holes in both layers, respectively. Combining red and blue-green lights, emitted from the ncSi and the polymer layers, respectively, produces the emission of white electroluminescence. Herein, a hybrid-WLED with a sufficiently low turn-on voltage (3.5 V), produced by taking advantages of the large Stokes shift inherent in ncSi, is demonstrated.

1. Introduction

Solid-state lighting in the form of light emitting diode (LED) which would reduce global energy consumption and green house gas emission is very much promising in lighting industry.[1,2] A variety of phosphor-coated chips controls the currently commercialized LEDs. In the fabrication of those devices, a common approach is to down-convert blue, violet or ultraviolet light into longer-wavelength light by using phosphors including rare earth-doped materials, nanocrystals of quantum dots (ncQDs) and organics.[3–8] The ever-increasing demand for facile, convenient and low-cost performance has sustained a continuous effort to develop new phosphors; however, this type of LEDs is confronted with its fundamental limit that luminance is closer to its saturation with excitation in addition to other drawbacks including an indispensable backlight. In contrast, the electric driven LEDs offer advantageous properties including the device-structurally admissible heavy-carrier-injection compared to the phosphor-coated devices although the improved efficiency of emission is still challenging theme.[9–11] It is well known that the use of compound semiconductors such as InGaN and InGaP allows the fabrication of red-green-blue (RGB) electroluminescent (EL) devices. Yet the development in manufacturing diode-junction-device for white light emission lags due to electronic structures inherent in compound semiconductor nanostructures.[12,13] Specifically, a direct bandgap structure featured to compound semiconductor QDs gives small Stokes shift between optical absorption and emission, resulting in a band-edge emission.[14–17] This unique optical character provides an advantage for certain applications, but serves as a disadvantage for manufacturing of white LED (WLED). For example, the small Stokes shift often causes the charge carrier transfer between neighboring different size QDs of the diode emissive layer. This phenomenon leads to the non-radiative transfer from a donor QD to an acceptor QD without emission of a photon. In this situation, we are no longer able to see white light emission from the device. Considerable efforts have been taken to date to minimize such an undesired charge carrier transfer. In addition to the shape control of QDs, the

Dr. B. Ghosh, Dr. Y. Wakayama, Dr. N. Shirahata
International Center for Materials
Nanoarchitectonics (WPI-MANA), 1-1 Namiki
Tsukuba, 305-0044, Japan
E-mail: SHIRAHATA.Naoto@nims.go.jp

Dr. Y. Masuda
National Institute of Advanced Industrial Science
and Technology (AIST)
2266-98 Anagahora, Shimoshidami, Moriyama
Nagoya 463-8560, Japan

Dr. Y. Imanaka
Nano Physics Group
NIMS, 3-13 Sakura
Tsukuba 305-0003, Japan

Dr. J.-i. Inoue
Material Properties Theory Group
NIMS, 1-1, Namiki 305-0044, Japan

Dr. K. Hashi, Dr. K. Deguchi, Dr. S. Ohki, Dr. T. Shimizu
High Field NMR Group, 3-13 Sakura
Tsukuba 305-0003, Japan

Dr. H. Yamada, Dr. Y. Sakka
Advanced Ceramics Group
NIMS, 1-2-1 Sengen, Tsukuba 305-0047, Japan

Dr. N. Shirahata
PRESTO, Japan Science and Technology Agency (JST)
4-1-8 Honcho Kawaguchi
Saitama 332-0012, Japan

DOI: 10.1002/adfm.201401795

doping of metals ions into QDs is also a candidate to eliminate the obstacles because of enlarged Stokes shift; however, these structural changes of QDs have little drastic effect on its enlargement.[18–20] Unlike the structural control of QDs, Won et al. reported the customized device design, in which respective emission regions are patterned, to forbidden the charged carrier transfer.[21] Thus, the structural design of WLED is still challenging subject to achieve efficient light emission.

In this article, we simply replace the QDs by silicon nanocrystals (ncSi) to manufacture a WLED device. A key to solve the problems lies in the use of an enormous large Stokes shift between optical absorption and emission, which is an unparalleled feature inherent to ncSi with diamond cubic lattice structure. Specifically, it is known that control over structure of ncSi gives continuous tuning of photoluminescence (PL) in a wide wavelength ranging from 300 nm to 1060 nm. The excitation maxima for those emissions absolutely appear in the near-ultraviolet region.[22–28] The large window between absorbance and emission is available for other color component without any intervention. We expected that the efficient superimposition of emission spectra produce a pure white light emission and its color rendering. A few groups have fabricated ncSi based LEDs and reported more recently size tunable emission wavelength from 600 to 900 nm in hybrid device structure.[29–31] In the present article, we first demonstrate hybrid WLED devices using suitable thin film of ncSi and organic polymer, working at a sufficiently low turn-on voltage suitable for future industrial use.

2. Results and Discussion

2.1. Synthesis and Characterization of ncSi

Synthesis of strongly luminescent ncSi is also one of challenging subjects. There are two approaches to achieve the highly efficient red-light emissions such as 1) plasma synthesis with Ar-SiH_4-H_2 gaseous system,[32] and 2) thermal treatments of hydrogen silsesquioxane (HSQ) or sol–gel hydrosilicate glasses derived from trichlorosilane.[24,25,33] The latter approach does not require any special tools for synthesis, but a reducing atmosphere such as a 5%–H_2/95%–Ar gaseous system for thermal decomposition of the hydrosilicate glasses.[25,34] In addition, the costly HSQ is better to be replaced by any alternatives to expand the general versatility of this chemical route. These obstacles motivated us to modify the route in which the efficiently emitting ncSi are synthesized under milder conditions than the previous methods.

Triethoxysilane (TES) is commercially available, inexpensive, non-hazardous, and solution processable even under ambient air. First, we prepared a glossy white TES-derived sol–gel powder by adding a mixture of 18.2 MΩ/cm water and HCl into TES molecules. Then, we characterized the powder by X-ray photoelectron microscopy (XPS) and Fourier transform infrared (FT-IR) spectroscopy to determine its chemical composition. A survey spectrum of XPS confirmed that the powder is composed of Si, O and C atoms. According to a narrow spectrum of Si2p region, there is a single peak at 102.3 eV corresponding to three-valent Si (see Figure S1, Supporting Information). A FT-IR spectrum showed the presence of three vibration modes ascribed to H–Si–O, O–Si–O and Si–H bonds (see Figure S2, Supporting Information). These spectroscopic studies indicate the formation of $HSiO_{1.5}$ according to:

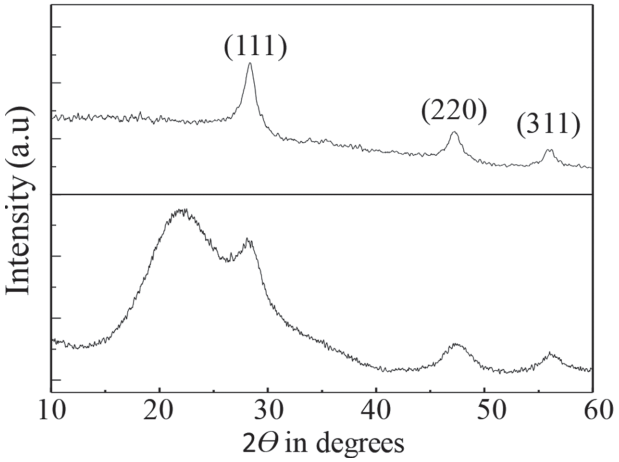

Figure 1. XRD patterns of thermal processed TES derived sol–gel glasses before HF etching (lower panel) and after hydrosilylation of 1-octadecene followed by purification (upper panel).

$$4HSi(OCH_2CH_3)_3 + 6H_2O \rightarrow 4HSiO_{1.5} + 12CH_3CH_2OH \quad (1)$$

Absence of other signals in the Si2p region confirmed that the powder is only composed of $HSiO_{1.5}$. The $HSiO_{1.5}$ powder was then heated at 1100 °C for 1.5 h in a simple N_2-flow condition with a conventional muffle furnace. The white powder of $HSiO_{1.5}$ turned metallic black during heating. Both a major crystalline phase and a chemical bonding state of the black powder were characterized by X-ray powder diffraction (XRD), XPS and FT-IR. A lower panel of **Figure 1** shows XRD pattern. A very broad diffraction with a peak maximum at around $2\theta = 22°$ is attributed to amorphous silica. On the other hand, we see characteristic diffraction signals corresponding to the (111), (220) and (311) reflections of diamond cubic lattice of Si. The broadening of the diffraction peaks appears due to the small size of the crystals. Typically, an average crystal diameter was 6.5 nm based on the Scherrer broadening of the XRD spectrum. XPS spectrum of the Si2p region has two strong peaks at around 99 eV and 103 eV, corresponding to zero-valent and four-valent Si, respectively (Figure S3, Supporting Information). In the FT-IR profile, there are only two broad peaks attributed to Si–O–Si (1090 cm^{-1}) and Si–OH (791 cm^{-1}) bonds. On the other hand, we also see the disappearance of Si–H and H–Si–O bonding states in the black powder (see Figure S4, Supporting Information). The combined structural analysis implies that $HSiO_{1.5}$ disproportionate into metallic Si and SiO_2 at 1100 °C in N_2 atmosphere by the following equation:

$$4HSiO_{1.5} \rightarrow Si + 3SiO_2 + 2H_2 \quad (2)$$

Because of gaseous hydrogen generated during the reaction, some of the black powder spilled out of the quartz vessel. According to the Equation 2, the elemental Si assembles to form a diamond cubic lattice of ncSi embedded in SiO_2 matrix. The ncSi terminated with hydrogen atoms (ncSi:H) were collected

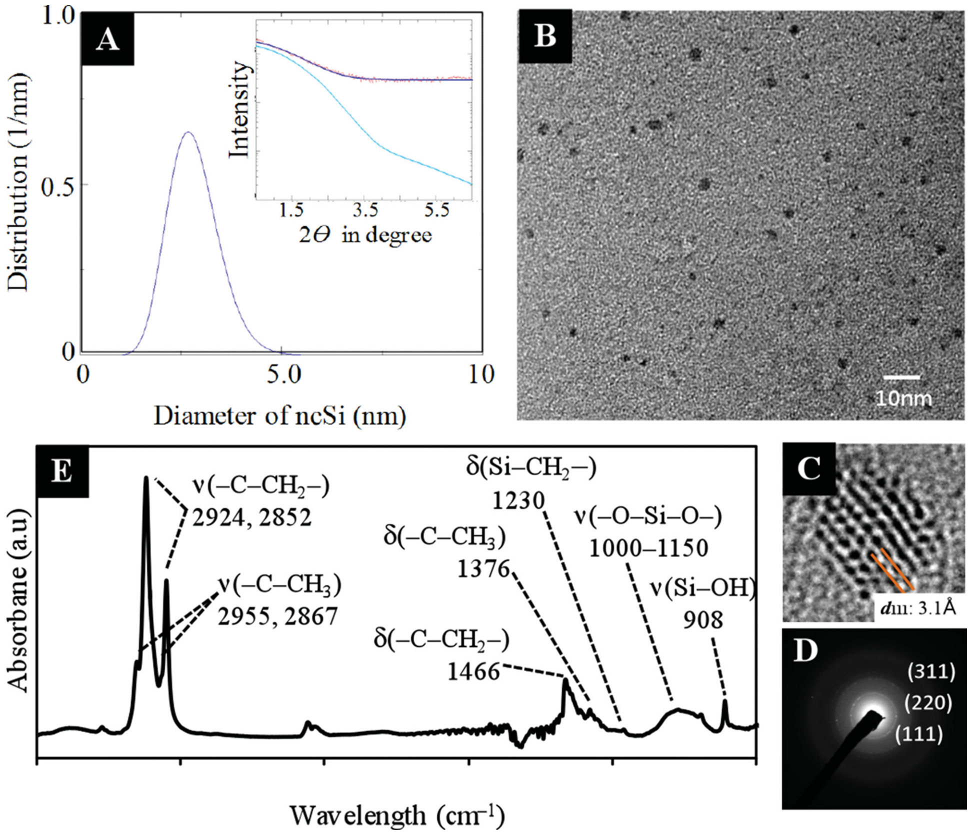

Figure 2. A) Size-distribution of the nsSi-OD sample estimated by SAXS. In the inset, the experimental data drawn with red-line is plotted together with the simulation pattern drawn with blue-line for SAXS analysis. B) Low magnification and C) high magnification TEM images with D) SAED pattern, E) FT-IR spectrum of the ncSi-OD sample.

by etching with hydrofluoric (HF) acidic solution, followed by a simple centrifugation. On the surface of ncSi, there are monohydride (SiH at 2086 cm^{-1}), dihydride (SiH_2 at 2108 cm^{-1}), and trihydride (SiH_3 at 2137 cm^{-1}) species, which were confirmed by FT-IR spectrum (Figure S5, Supporting Information). Next, the surface of ncSi:H was terminated with alkane monolayers by thermal hydrosilylation of 1-octadecene. An upper panel of Figure 1 shows XRD pattern of the sample prepared by hydrosilylation of 1-octadecene. Obviously, the characteristic (111), (220), and (311) planes become prominent. The amorphous silica derived from the heated $HSiO_{1.5}$ was removed from the black powder within 1 h of HF etching.

Small angle X-ray scattering (SAXS) is a powerful tool for rapid and precise evaluation about a polydispersity of single-nanoscale particles in a form of solid or liquid. We preferred the SAXS technique to measure the size distribution of the ncSi modified with octadecane monolayers (ncSi-OD). We measured the ncSi-OD sample in both solution form and powder form with SAXS. Assuming that the ncSi are round-shape, the SAXS data was fitted with Gaussian distribution. The analysis gave a distribution profile with a narrow spectral line width as shown in **Figure 2**A. The estimated average size of ncSi was typically 2.6 nm. To avoid the ligand effect, we also measured SAXS of the ncSi-OD sample in powder form. The measured average size of the powder sample was around 2.1 nm. A representative low magnification TEM photograph is shown in Figure 2B. The ncSi have spherical shape, and the average size was estimated to 2.1 nm which is quite well matched with the size distribution obtained by SAXS measurement. Figure 2D shows a typical selected area electron diffraction (SAED) pattern taken from the observation area containing the ncSi in Figure 2B. In the SAED pattern, each ring correspondingly satisfies the Bragg conditions for crystalline phase. The SAED pattern exhibits three diffraction rings corresponding to (111), (200), and (311) planes, again confirming that the contrasted dots in the image correspond to ncSi with diamond cubic lattice structures. These analytical results is consistent with the fact that 2.1 nm of size is large enough to give a diamond lattice structure of ncSi.[35] Figure 2C shows a representative high-resolution image of ncSi. The lattice spacing was approximately measured to be 0.31 nm, which matches with *d*-spacing of (111) plane of diamond cubic lattice of Si. Surface chemistry of the ncSi was studied by FT-IR as shown in Figure 2E. The spectrum was dominated by characteristic C–H stretching (2850–2952 cm^{-1}) and bending/scissoring (1376 cm^{-1} and 1466 cm^{-1}) attributed to the surface-bonded alkyl groups.[36] The infrared absorption attributed to terminal double bonds of ligands is never seen in the spectrum. Instead of disappearance of the absorption at 2100 cm^{-1}, the appearance of a small peak at 1230 cm^{-1} indicates the successful replacement of Si–H bond by Si–C bond.[37,38] There is a low intensity peak around 1000–1150 cm^{-1} which are correspond to Si–O–Si vibrations. Although the oxidized surface

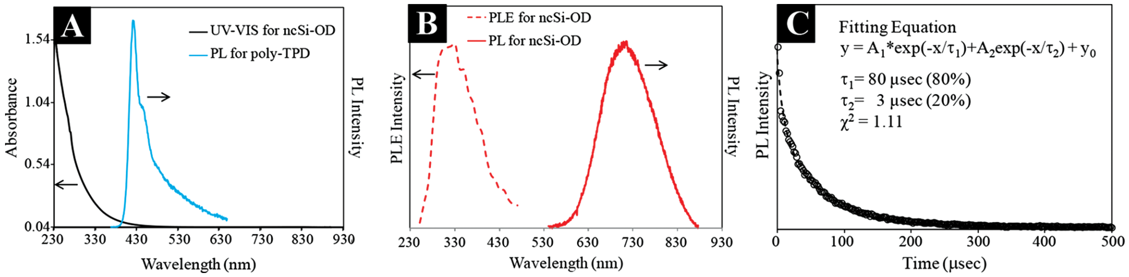

Figure 3. A) UV–VIS spectrum of the ncSi-OD sample and PL spectrum of the poly-TPD sample excited with 370 nm light. B) PLE and PL spectra of the ncSi-OD sample. PLE spectrum was obtained for the emission maximum of 710 nm. C) PL decay curve (λ_{ex} = 310 nm, measured at the emission maximum) of the ncSi-OD sample. The best fit was carried out using bi-exponential decay function (χ^2 = 1.11) τ: lifetime, and the contribution ratios for the curve fitting are noted in parentheses.

areas were remained even after hydrosilylation, the relatively high packing density of surface monolayers imparts the surface of the nanocrystals hydrophobicity. For example, the ncSi-OD sample moved on a TLC plate in the eluent of hexane at almost the same speed as 1-octadecene, and was highly soluble in non-polar solvents.

2.2. Photophysical Characterization

Photophysical properties were investigated using thin film formscoated on quartz substrates. **Figure 3** shows optical absorption and PL spectra of a thin ncSi-OD film. PL spectrum of a thin poly[*N,N*'-bis(4-butylphenyl)-*N,N*'-bis(phenyl)benzidine] (poly TPD) film was used for reabsorption study because poly TPD act as not only hole transporting layer but also blue-green emitting layer in our device. In Figure 3A, we see a featureless optical absorption spectrum with an absorption edge at around 350 nm, resulting in a high light transparency at the visible-NIR (≈930 nm) region. The PL spectrum of the poly TPD sample expresses the rapid increase starting at 390 nm to give a broad emission spectrum covering over the VIS range, in particular 400–550 nm. We took particularly note of this very little overlapped spectral area between the optical absorption spectrum of the ncSi-OD sample and the PL spectrum of the poly TPD sample. Owing to this small spectrum overlap, we are firmly convinced that the ncSi-OD layer must not absorb the light emitted by the poly TPD layer when those are sandwiched as a device active region of WLED.

Figure 3B shows PL and PLE spectra of the ncSi-OD sample. As seen in the PL spectrum, an emission peak appears at around 710 nm when excited with 320 nm light (excitation maximum). A full width half maximum (FWHM) of the PL spectrum was about 150 nm. The CIE (Commission Internationale de I'Eclairage) coordinate values (x, y), (0.56, 0.28), corresponding to the red region of visible light, as evidenced from the CIE diagram in Figure 6B. It should be noted that the fluorescence emission band shift with the wavelength of the absorption edge is approximately 360 nm. This extraordinary Stokes shift is the crucial differences between ncSi and ncQDs of compound semiconductors with a band-edge emission feature. The estimated PL QY of the ncSi:H sample was typically 1%, which is quotidian value for ncSi. However, only by hydrosilylation of 1-octadecene on the ncSi:H PL QY dramatically increased up to 25%. A time-resolved PL spectrum was measured to explore the *e-h* carrier recombination dynamics in the ncSi-OD at room temperature (see Figure 3C). An experimental decay plotted by small open circles can be satisfactorily fitted well the theoretical curve of the bi-exponential function with two time constants τ_1 and $\tau_{2.}$ The curve was almost dominated by slow decay component, τ_1 = 80 μs which is as long as PL lifetimes measured using ncSi samples with diamond lattice structures synthesized under the reaction conditions supplying a high crystallization energy.[39–41]

Both the large Stokes shift between absorbance and emission and the slow PL decay could be discussed as a result of indirect bandgap structure inherited even in nanostructures.[42] Nevertheless, the estimated PL QYs of ncSi-OD samples are high without any exception, resulting in the complicated debate on their luminescence origin. Aside from this discussion, we noticed an unparalleled advantage that such a large Stokes shift possibly does not cause the energy transfer from the poly-TPD layer to the ncSi-OD layer but contributes to create a continuous PL spectrum by stacking complementary the emission colors from each layer in our device active region.

2.3. Current–Voltage Characteristics

We fabricated prototypes of WLED device based on a device design illustrated in **Figure** 4A. The device active regions are commonly composed of two emissive layers, that is, poly-TPD and ncSi-OD layers. In the present study, we found that thicknesses of each emissive layer are the most important key to control over the color rendering properties of white light emitted by the devices. Therefore, we used atomic force microscopy (AFM) to measure the accurate thicknesses of the layers. Thin ncSi-OD films casted on the quartz glass in a manner to the device fabrication were carefully scratched, and measured by AFM. Figure 4B shows a typical topographic image of the scratched ncSi-OD films. As is more commonly seen in such a topographic image, we see the vicinity of the scratched region slightly thickens due to the disturbance caused by the scratch. Figure 4C shows a depth profile along the white dashed line in the topographic image of Figure 4B. The depth of the valley with reference to the uniform film was determined as a thickness of the ncSi-OD film. In all the prototypes of WLED device demonstrated herein, we used 20 ± 2 nm thick poly-TPD layers.

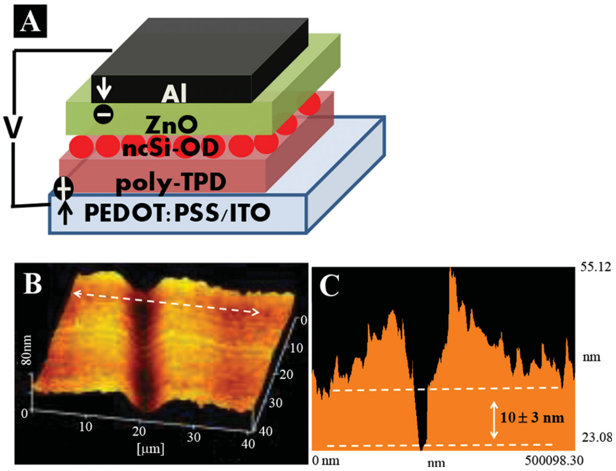

Figure 4. A) A design of WLED device with a hybrid emission layer. B) A topographic image of the scratched ncSi-OD layer for measuring film thickness, and C) The depth profile of the surface along the white line is shown. Average thickness is estimated from the different heights of the film in two different side of the debris caused by the scratch.

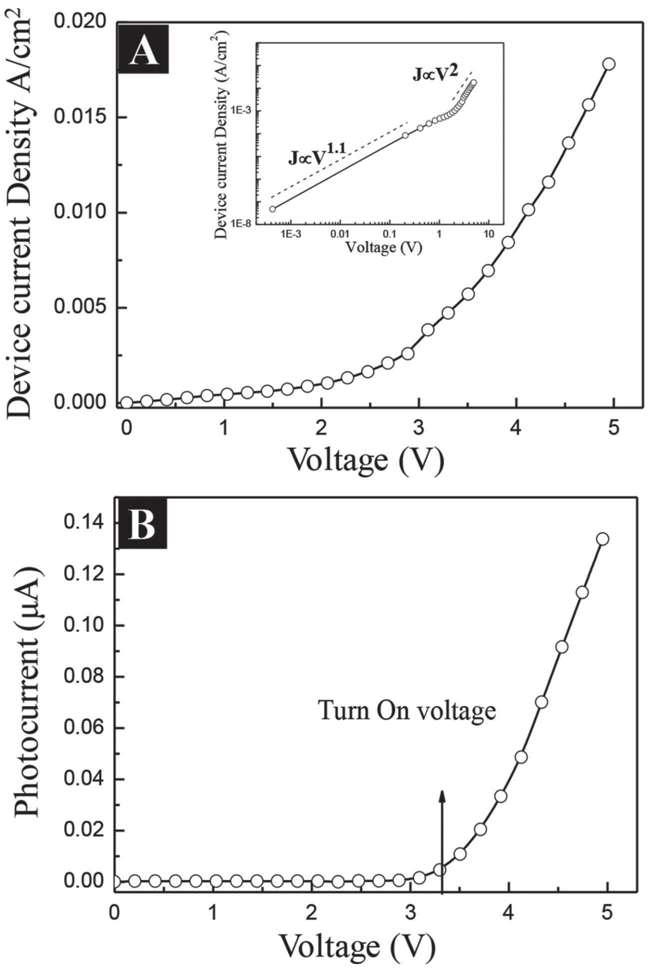

Figure 5. A) Device current density versus voltage plot of the device. The inset shows a Log–Log plot of the device current density versus voltage characteristic. B) Photodetector current versus voltage plot of the device indicating turn-on voltage.

Whereas the thicknesses of the ncSi-OD layers were varied for three different values; estimated as 10, 25, and 50 nm with standard deviation of 3 nm for each (see also Figure S6, Supporting Information).

Current density-voltage characteristics were investigated using our prototypes of WLED devices. **Figure 5**A shows a typical characteristics of the device current density as a function of voltage when we used a device with a 10 nm-thick ncSi-OD layer, which is the best thickness so far for emission color close to the pure white. Figure 5B shows a calibrated photocurrent–voltage characteristic of the same device. At 3.5 V, photodetector current starts to increase exponentially its current value from the dark noise current. That voltage is threshold voltage often called "turn-on voltage". It should be noted that this value of turn-on voltage is very low compared to the hybrid WLED devices reported in previous literatures due to the following two possible reasons. First, there is no energy transfer of photon between the poly-TPD layer and the ncSi-OD layer as we expected. Second, the ncSi surfaces are not encapsulated with silica shells, which serve as insulator.

To investigate further on the conduction mechanism we plot *J*–*V* characteristic double-logarithmic scale, shown in the inset of Figure 5A. From the curve, the calculated slope follows a power law behavior, $J \propto V^n$. In a low voltage bias regime, the conduction could be described by the Ohmic conductance behavior ($n \approx 1$). In this regime, the pre-existing bulk free carriers whose density is invariant and independent of bias voltage are dominant over the injected charge carriers. On the other hand, we see an obvious transition of the charge conduction mode from Ohmic to space charge limited (SCL) conduction at ~2.5 V. This transition behavior was reported in 1950s by Lampert.[43] Specifically, assuming that a semiconductor is charge-trap-free or is forbidden to use any traps for its internal carrier transport, the current density limited by the SCL conduction mechanism is proportional to square of voltage, that is, $J \propto V^2$ (see the double-logarithmic *J*–*V* plot in the inset of Figure 5A). Under the presence of unoccupied charge-traps for carrier transport, the *J*–*V* relation could be described as $J \propto Vm^{+1}$; where m is a parameter related to distribution of trap states in a semiconductor.[44,45] By plotting *J*–*V* relation in log–log scale, the value of exponent "*n*" was estimated from the slope of the straight line. (see Figure S7, Supporting Information). The charge-trap-free SCL conduction regime we see a slope of 2 ($n = 2$), while the imperfect SCL conduction behavior caused by exponentially distributed traps gives a slope of $n = m + 1 > 2$. The *J*–*V* characteristics for three devices with different thicknesses of ncSi-OD exhibit respective linear portions of $1.05 < n < 1.1$ in a low voltage bias regime, resulting in Ohmic conduction (see Figure S7, Supporting Information). Current density is linearly proportionate with applied voltage (V), that is, $J \propto V$. In a higher bias regime, the magnitude of SCL conduction depends on the thickness of ncSi-OD layer. For a device with a 10 nm thick ncSi-OD layer, we see perfect SCL conduction behavior because of a slope of 2. On the other hand, the current density curve becomes steeper under increasing applied voltage for other two samples, that is, $n \approx 2.8$ and ≈ 3.2 for each device with a 25 nm thick and a 50 nm thick ncSi layers respectively. These SCL conduction behaviors with slopes more than 2 could appear due to difference in amount of charge-traps for carrier transport.

2.4. Electrolumiescence Characteristics

An operation mechanism of a hybrid LED device with an organic/colloidal ncQD multilayer has been proposed by Madigan and co-workers.[46] The ncQD layer is composed of a direct bandgap semiconductor such as CdSe in which a free exciton generates even at room temperature because of its exciton binding energy larger than thermal energy $k_BT \approx$ 30 meV. Photon generation for EL output occurs in the ncQD layer via two carrier transition processes: 1) direct injection of electrons and holes into the ncQD layer from electrodes and 2) Förster energy transfer from the organic layer to the ncQD layer.[47] The later process is much responsible for color of EL output from the organic/colloidal ncQD multilayer. Owing to a small Stokes shift between absorption and band-edge emission energies, the ncQD layer reabsorbs its own emission and/or the emission of short-wavelength light from the adjacent organic layer through exciton energy transfer. As a result, the color of EL output to the naked-eyes depends on the magnitude of fundamental bandgap of the ncQD.[48]

In the present study, we replaced the ncQD by the luminescent ncSi-OD, which exhibits a large Stokes shift between absorption and emission, to minimize a risk of reaborption just described. This substitution gave a promise that by avoidance of the risk of the particular concern we see a composite EL spectrum of the ncSi-OD layer that is superimposed on an emission spectrum of the poly-TPD layer.

Next issue was the design of a device structure in which the excited carriers recombine in both the ncSi-OD and the poly-TPD layers for giving respective EL emission. To resolve this issue, we focused on control over thicknesses of the constituent layers. As a model experiment, we fabricated three prototypes of WLED device in which different thicknesses of the red-luminescent ncSi layers are sandwiched between the poly-TPD and the ZnO layers as shown in Figure 4A. All of EL outputs were measured in ambient conditions without any atmospheric control under the risk of a poor device performance. **Figure 6**A shows EL spectra of the devices with 10, 25, and 50 nm of the ncSi-OD layers, and the corresponding CIE chromaticity coordinates are shown in Figure 6B. A device without ncSi-OD layer served as a standard shows a broad EL spectrum covering over the 400–600 nm range of visible light wavelength as depicted with a black data. Its emission spectral features including shape and emission maximum corresponds to those of a poly-TPD film, which has a chromaticity coordinate of (0.25, 0.34) in bluish green region of visible light as evidenced from Figure 6B. Interestingly, the addition of ncSi-OD layers into a device active region gives a significant change in EL spectral features. A device with a 50 nm-thick ncSi-OD layer shows EL spectrum as depicted with green line in Figure 6A. A strong peak centered at 710 nm dominates the EL spectrum, but we see a very small and broad peak covering over the 400-600 nm range. As a result, the EL spectrum could be described as the poly-TPD emission spectrum superimposed upon the ncSi-OD emission spectrum. Even this small spectral contribution from the poly-TPD layer gives a big shift in chromaticity coordinate of the EL spectrum in comparison to that of (0.56, 0.28) which is estimated from the device with only a ncSi-OD layer. As plotted in Figure 6B, the chromaticity coordinate of the resultant EL becomes (0.42, 0.29), which looks like reddish white rather than red or pink colors. Decrease in thickness of the ncSi-OD layer increases the compositional ratio in EL intensity of the blue-green emission to the red emission. For example, a device with a 25 nm-thick ncSi-OD layer shows EL spectrum where a spectral contribution of the blue-green emission increases whereas that of the red emission is suppressed as thickness of the ncSi-OD layer is decreased (see blue line in Figure 6A), giving a chromaticity coordinate of (0.35, 0.29). The coordinate positions within the white region but slightly inclined towards the red luminescence region. Finally, our design of LED device has emitted the quasi pure-white light when the thickness of the ncSi-OD layer was adjusted at ≈10 ± 3 nm. As depicted by a red-line in Figure 6A, the EL spectrum spreads over the entire visible range generating light close to pure-white in color, and has chromaticity coordinate of (0.32, 0.31) as its evidential value. The device has emitted a similar white light when applied at 3.5 eV or more. Although it has not yet been succeeded in casting a uniform ncSi-OD layer with a thickness thinner than 10 nm, we have worked out measurement of EL spectrum of a device in which the ncSi-OD are non-uniformly distributed to form a red luminescent layer thinner than 10 nm (see Figure S8, Supporting Information). Owing to the non-uniform ncSi-OD layer, the operation voltage of the device was high, but the resultant EL spectrum has chromaticity diagram of (0.26, 0.33).

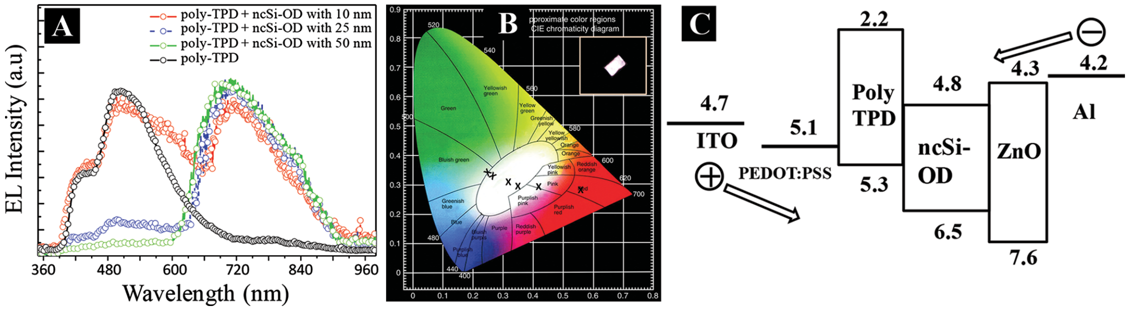

Figure 6. A) EL spectra of the devices with and without ncSi-OD layers (for three different thickness) at the applied bias 3.5 V and 4.5 V, respectively. B) CIE diagram showing chromaticity coordinates of a device with only poly-TPD layer in the device active region, a device with only ncSi-OD layer in the device active region, and the devices with both the 20 nm-thick poly-TPD layer and the ncSi-OD layers (*d* thickness = 50, 25, 10, and <10 nm). A typical digital photograph (the inset, 2 mm × 1 mm) of white light to the naked eyes from WLED device with a 10 nm ncSi-OD layer at the applied bias 4.0 V. C) The proposed energy diagram of the WLED device at zero field.

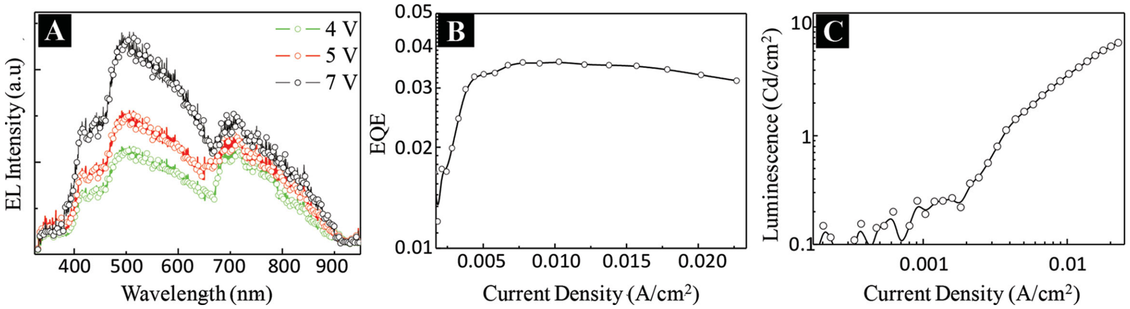

Figure 7. A) EL spectra at three different bias voltages. B) External quantum efficiency (EQE) versus device current density. C) Luminance versus device current density in log–log scale of the WLED device.

This coordinate value locates within white region close to the boundary with bluish green luminescence region, suggesting the successful tuned EL spectrum described as blue-green component from poly-TPD layer, which is superimposed upon red EL component from the ncSi-OD layer. A series of EL measurements provides the direct evidence that each white light emission spectrum is composed of the blue-green EL from the poly-TPD layer and the red EL from the ncSi-OD layer. Furthermore, the compositional ratio in thickness of each layer depends on color rendering properties of white lights.

Next, we discuss the carrier transition processes to give the successful emission of white lights. The proposed energy level diagram of the WLED device under applied zero bias is shown in Figure 6C to discuss the possible carrier transfer. Several parameters such as work function (Φ), band gap (E_g), ionization energy (IE), and electron affinity (EA) of ITO ($\Phi = -4.7$ eV), PEDOT:PSS (IE = −5.1 eV), Al ($\Phi = -4.2$ eV), poly-TPD (E_g = 3.1 eV and IE = −6.3 eV), and ZnO (IE = −2.4 eV and EA = −7.3eV) were taken from the literature.[49] The IE of the ncSi-OD was estimated to approach −6.5 eV from the ultraviolet photoemission spectroscopy (UPS) spectrum. The EA of the ncSi-OD is calculated at −4.8 eV on the basis of assumption that the fundamental optical gap generates red light emission. Based on the band diagram and the intrinsic character of ncSi, only the direct charge injection could contribute the white light emissions demonstrated here. Both electrons and holes are injected from each contact into the device active region. The electrons are injected from the Al contact through the ZnO electron-transporting layer to the ncSi-OD layer due to the energy alignment of the conduction band minima of the ncSi-OD and ZnO layers, thereby producing the electron-rich ncSi-OD layer. A poly-TPD layer serves as a good electron blocker. If a ncSi-OD layer is sufficiently thick, the electrons injected from a contact must be trapped only on the ncSi-OD layer. However, we chose the ncSi-OD layers that are thin to traverse the carriers up to the neighboring poly-TPD layer through a slope of energy gradient at this junction. On the other hand, the holes are injected from ITO contact through the PEDOT:PSS layer into the device active region. ZnO layer serves as a good hole blocker, and prevents from the *e-h* carrier recombination in the metal Al electrode. The magnitude of hole injection barrier between the poly-TPD layer and the ncSi-OD layer is approximately 1.2 eV. The holes are injected from the anode into the ncSi-OD layer under the increasing applied voltage, but some could remain and recombine in the poly-TPD layer. Therefore, both electrons and holes eventually meet in both the ncSi-OD layer and the poly-TPD layer simultaneously, and radiatively recombine for respective EL output and subsequent spectral superimposition. Increase in thickness of the ncSi-OD layer suppresses the leak of electrons into the poly-TPD layer, resulting in the decrease of the EL spectral contribution originating from the poly-TPD layer. This is completely consistent to the resultant EL spectra in Figure 6A. We therefore concluded that such unique white EL phenomena are observed under limited conditions in which the thickness ncSi is severely controlled at 50 nm or thinner.

The emission spectra from the WLED devices exhibit voltage dependence. **Figure 7**A shows the EL output spectra under different bias conditions. The spectral profile at 4 V bias whereas the luminance contribution from the poly-TPD and the ncSi-OD is nearly equal. As the voltage increases the spectral contribution from poly-TPD increases. In contrast, the ncSi-OD emission is less contributing in the spectra. As a result, the blue-green emission spectra originating from poly-TPD layers grow under increasing applied bias voltage. The emissions from ncSi-OD layers did not increase and saturated due to a low efficiency of carrier injection into the ncSi-OD layers. The further extension of the electron range into the underlying poly-TPD region leads to dominant blue-green emission in the LED output spectrum for a high injection current density. In the high enough bias, high energetic carriers penetrate and traverse up to poly-TPD layer crossing the barrier height. As a result, the *e-h* recombination process increased in poly-TPD region to give the increase of blue-green EL, while the ncSi-OD layer saturates.

We measured photocurrent as white EL output with a photodetector to estimate the external quantum efficiency (EQE), and plotted the values in Figure 7B as a function of the injected current density. EQE was estimated by the following equation:

$$\mathrm{EQE}(\%) = \frac{\left[I(\mathrm{ph}) - I(\mathrm{d})\right] \times q}{R \times I \times E(\mathrm{photon})} g \times 100$$

where I(ph) is the photocurrent detected by photodiode (Hamamatsu S1336-8BQ), placed just below the EL device. I(d) is the dark current of the photodiode, when the device is not operative. I is the device current, R is the responsivity of the photodiode, q is the charge of electron, "E (photon)" is the photon energy, and g is the configuration factor of our measurement set up, which we estimated was 0.3. A comparison of the photodetector current for other devices has been shown (see Figure S9, Supporting Information). For the thicker ncSi-OD layer, the turn-on voltage slightly increased. The peak value of EQE of our device was estimated 0.035. This efficiency was compared with the values of EQE of the QD-WLED devices. Those WLEDs have the device active regions of QDs such as core/shell/shell ZnSe/CdSe/ZnS nanocrystals. The estimated EQE values of the WLED devices lie in the ranging from 0.033 to 0.36.[9,11] Our efficiency of EQE is well comparable with the previously reported values of the QD-WLEDs. Various structural parameters of devices influence on the values of EQE. In order to improve EQE, we will develop a dense ncSi film as a device active region in addition to the band alignment of the layers for the efficient charge transport. Overall, the values of the EQE were low, but the EQE increased with device current; the EQE shows a trend of a decline at higher device current evidencing the effect of heat generated in the devices. The decline in the EQE might also occur due to an increase in Auger-type nonradiative decay of the e-h carriers or imbalance in e-h injections leading to space-charge build-up in the devices.[50,51] While the *I*–*V* characteristics are expectedly nonlinear in nature, the luminance-current plots show that luminance was detectable above a threshold current as shown in Figure 7C. Above the threshold value, the luminance-current density plot is linear in some region and after that at very high current we can see a tendency to decline of that rate in double-logarithmic scale.

3. Conclusion

A new hybrid device structure was proposed to fabricate white light emitting diodes (WLED). All spectra of white lights were produced by spectral-superposition of red light from the ncSi-OD layer and blue-green light from the poly-TPD layer in the device active regions of diodes. The red-color luminescent ncSi-OD was prepared by the improved disproportional reaction of triethoxysilane-derived sol–gel glasses under nitrogen atmosphere followed by hydrosilylation of 1-alkenes. By taking advantage of a large Stokes shift featured to the ncSi-OD layer, the photon for EL was generated through the direct injection of electrons and holes into the active device regions from electrodes whereas Förster resonance energy transfer between adjacent emissive layers was suppressed, leading to the successful spectral-superposition for producing the white emission spectra. The another advantage of our device is a low turn-on voltage for its operation. ZnO worked as a good inorganic stable *n*-type electron injecting layer, and also served as a good hole blocker. The proposed design of devices offers a potential to produce a quasi spectrum of sunlight. It is known that the ncSi is environmental friendly and nontoxic.[52,53] The present work discloses at the first time WLED with the earth abundant Si avoiding toxic Cd, Pb, As based structure and a simple fabrication process along with a systematic analysis of the device operation.

4. Experimental Section

Reagents and Materials: Triethoxysilane (TES) was purchased from TCI chemicals. Electronic grade hydrofluoric acid (49% aqueous solution, Kanto Chemical), HPLC grade toluene, dicholrobenzene, ethanol, methanol and mesitylene were purchased from Wako chemical. Poly-TPD, (LumTech), 1-octadecene, zinc acetate dehydrate, PEDOT:PSS solution (Sigma-Aldrich) were used as received.

Si/SiO_2 Composite Preparation: In a typical synthesis, 5 mL of TES (6.0 g, 45 mmol) was added to a round-bottom flask equipped with a magnetic stir bar and stirred in Ar atmosphere using standard Schlenk techniques. HCl solution (water : HCl = 3:1) (1.59 mL) was added drop wise slowly to the TES placed at the bottom of flask. After some time xerosol was formed and then the gel was dried in vacuum for overnight. The dried white solid precursor was placed in a quartz crucible and transferred to a high-temperature tube furnace. Samples were thermally processed in N_2 flow condition using a simple muffle furnace. Final temperature 1100 °C was reached at step 10 °C/min and stayed 1.5 h at 1100 °C. After cooling to room temperature, the resulting dark brown solid products were mechanically ground in a mortar and pestle to yield fine, free-flowing powders.

Preparation of Luminescent ncSi: 200 mg of the fine powder was mixed with 5 mL of ethanol, 5 mL of HF (48 %), and 5 mL of 18.2 MΩ/cm water. Then, the mixture was stirred for 1 h to achieve the acidic etching of SiO_2 matrix and the gradual decrease in size of core Si. The hydride-terminated ncSi (ncSi:H) was centrifuged at a rotation speed of 10 000 rpm, washed two times with ethanol, and transferred into an another schlenk flask with 5 mL mesitylene and 5 mL 1-octadecene. After the mixture was degassed for at least 1 h with Ar bubbling, the the hydrosilylation of 1-octadecene on the ncSi:H was carried out at 150 °C over night in Ar atmosphere. After the reaction, the resulting yellow solution was evaporated to remove mesitylene and then, centrifuged with a mixture of a good solvent (toluene) and a poor solvent (methanol) in several times to remove unreacted 1-octadecene. In order to confirm the successful hydrosilylation, the product was examined by thin-layer chromatography (TLC) monitoring with hexane as an eluent. As expected, the ncSi moved at almost the same speed as eluent, suggesting the successful modification with octadecane menolayers. The purified ncSi samples were used for further characterizations and device fabrication.

Characterization: The size and morphology of the product was analyzed using high-resolution transmission electron microscope (HR-TEM, JEOL JEM-2100) operated at 200 kV and the selected-area electron diffraction (SAED) were performed along with the HR-TEM image. Major crystalline phase of the product was evaluated with X-ray powder diffraction (HT-XRD, RINT-TTR II and Reactor X, Rigaku, Japan) analysis operated in ambient air. Small-angle X-ray scattering (SAXS) data were obtained for solid-state ncSi. Measurements were performed in ambient conditions by transmission method on a Nano-Viewer of RIGAKU system using a rotating copper anode X-ray source operating at 40 kV and 30 mA with a PILATUS detector. A 3.0 mm of Beam stopper and 341.52 mm of camera length were employed. Film thicknesses were measrued at room temperature in ambient air by atomic force microscope (AFM; Seiko Instruments Inc., SPA-400, SPI-3800N) in dynamic force mode (DFM) using a Si probe (Seiko Instruments Inc., cantilever; force constant = 0.12 N/m). Structural phase of the product was also evaluated using a laser Raman microscope with 785-nm laser as excitation source (Raman-11, Nanophoton Corporation, Japan). FTIR spectrum was examined at 4 cm^{-1} resolution with 256 scans using FT/IR-4100 (JASCO, Japan). Optical absorbance spectra were recorded by UV–VIS spectrophotometer (JASCO V-650, Japan). PL measurements at room temperature were carried out with a spectrofluorometer (NanoLog, Horiba Jovin Yvon, Japan). Absolute PL QYs were measured by with an absolute PL QY measurement system (C9920-02, Hamamatsu Photonics, Japan). Time-resolved fluorescence decay profiles were recorded at room temperature on a time-correlated single photon counting (TCSPC) lifetime spectroscopy system in phosphorous mode with pulse laser diodes of λem = 370 nm (NanoLog, Horiba Jovin Ybon, Japan). The quality of the fit has been judged by the fitting parameters such as χ^2 (<1.4) as well as the visual inspection of the residuals.

Device Fabrication and Device Characterization: A 150 nm thin film of indium tin oxide (ITO) was uniformly sputtered on a soda-lime glass. A resistivity of the ITO film was measured to be less than 15 Ω/square. The ITO-coated glass substrates were first etched using HCl and Zn dust in a narrow strip. Then they were cleaned by ultrasonic agitation with a nonionic detergent, followed by in ethanol, in acetone and isopropanol and finally rinsed with 18.2 MΩ/cm water. After drying, the ITO-glass substrates were transferred to a reactive ion etching (RIE) chamber for plasma treatment, treated for 10 min under a pressure of 1 mTorr of nitrogen and oxygen mixture. Then PEDOT:PSS solution was first spin-coated onto plasma-treated substrates at a speed of 5000 rpm for 45 sec. Afterwards the PEDOT:PSS-coated substrates were loaded into Ar-filled homemade chamber, and baked at 140 °C for 30 min to eradicate any remaining solvent before the deposition of subsequent organic and ncSi layers. Poly-TPD was spun from chlorobenzene solution 10 mg/mL at a speed of 1800 rpm. The films were dried at 110 °C for 1 h in Ar environment. Solutions of ncSi in toluene (8 mg/mL) were then spun at three different speed 2000, 1200, 500 rpm to prepare three different thickness 10 nm, 25 nm and 50 nm film respectively. Less than 10 nm film was also prepared by spinning at 3000 rpm speed but the thickness was not successfully measured by AFM instrument by creating scratch. The films were dried in Ar environment at 130 °C for 1.5 h before deposition of ZnO as n type layer. ZnO was prepared by following reported procedure. ZnO layer was spin casted 30 mg/ml at a speed of 2000 rpm. Top electrode cathode aluminium (Al) was deposited by vacuum evaporation. The devices were characterized in a ambient condition. Current–voltage (*I–V*) characteristics were recorded with a computer interfaced Keithley 2425 electrometer, luminous output of the LEDs was measured with a calibrated silicon photodiode (Hamamatsu S1336-8BQ) coupled to a another computer interfaced Keithley 2400 electrometer in ambient air. Contact to the top Al cathode was made using Ag paste. EL spectra were measured using a computer interfaced Ocean Optics USB2000 fiber spectrometer. To determine the photometric brightness (cd/m^2) of the LED, the diode output power was first measured silicon photodetector that was directed at a fixed distance toward the ITO glass side of the LED. The LED luminance (brightness) was then calculated from the known portion of the forward emission and the LED output spectra.

Acknowledgements

This work was, in part, supported by JST-PRESTO, Grant-in-Aid for Scientific Research, Kakenhi (No. 26390024), MEXT, and the Konica Minolta Imaging Science Award from the Konica Minolta Science and Technology Foundation, Japan

Received: June 3, 2014
Revised: August 7, 2014

---

[1] M. H. Crawford, *IEEE J. Sel. Top. Quantum Electron.* **2009**, *15*, 1028.
[2] S. Pimputkar, J. S. Speck, S. P. DenBaars, S. Nakamura, *Nat. Photonics* **2009**, *3*, 179.
[3] V. Bachmann, C. Ronda, A. Meijerink, *Chem. Mater.* **2009**, *21*, 2077.
[4] H. S. Jang, H. Yang, S. W. Kim, J. Y. Han, S. G. Lee, D. Y. Jeon, *Adv. Mater.* **2008**, *20*, 2696.
[5] W. B. Im, N. George, J. Kurzman, S. Brinkley, A. Mikhailovsky, J. Hu, B. F. Chmelka, S. P. DenBaars, R. Seshadri, *Adv. Mater.* **2011**, *23*, 2300.
[6] B. Ghosh, M. Ogawara, Y. Sakka, N. Shirahata, *Chem. Lett.* **2012**, *41*, 1157.
[7] S. S. Babu, J. Aimi, H. Ozawa, N. Shirahata, A. Saeki, S. Seki, A. Ajayaghosh, H. Mohwald, T. Nakanishi, *Angew. Chem. Int. Edit.* **2012**, *51*, 3391.
[8] Q. L. Dai, M. E. Foley, C. J. Breshike, A. Lita, G. F. Strouse, *J. Am. Chem. Soc.* **2011**, *133*, 15475.
[9] P. O. Anikeeva, J. E. Halpert, M. G. Bawendi, V. Bulovic, *Nano Lett.* **2007**, *7*, 2196.
[10] W. S. Song, H. Yang, *Chem. Mater.* **2012**, *24*, 1961.
[11] Y. Zhang, C. A. Xie, H. P. Su, J. Liu, S. Pickering, Y. Q. Wang, W. W. Yu, J. K. Wang, Y. D. Wang, J. I. Hahm, N. Dellas, S. E. Mohney, J. A. Xu, *Nano Lett.* **2011**, *11*, 329.
[12] H. Q. Jia, L. W. Guo, W. X. Wang, H. Chen, *Adv. Mater.* **2009**, *21*, 4641.
[13] S. Nakamura, N. Senoh, N. Iwasa, S. I. Nagahama, *Jpn. J. Appl. Phys. Part 2 – Lett.* **1995**, *34*, L797.
[14] P. O. Anikeeva, J. E. Halpert, M. G. Bawendi, V. Bulovic, *Nano Lett.* **2009**, *9*, 2532.
[15] S. Coe-Sullivan, *Nat. Photonics* **2009**, *3*, 315.
[16] Q. Q. Dai, C. E. Duty, M. Z. Hu, *Small* **2010**, *6*, 1577.
[17] B. S. Mashford, M. Stevenson, Z. Popovic, C. Hamilton, Z. Q. Zhou, C. Breen, J. Steckel, V. Bulovic, M. Bawendi, S. Coe-Sullivan, P. T. Kazlas, *Nat. Photonics* **2013**, *7*, 407.
[18] T. Franzl, J. Muller, T. A. Klar, A. L. Rogach, J. Feldmann, D. V. Talapin, H. Weller, *J. Phys. Chem. C* **2007**, *111*, 2974.
[19] X. G. Peng, L. Manna, W. D. Yang, J. Wickham, E. Scher, A. Kadavanich, A. P. Alivisatos, *Nature* **2000**, *404*, 59.
[20] N. Pradhan, D. Goorskey, J. Thessing, X. G. Peng, *J. Am. Chem. Soc.* **2005**, *127*, 17586.
[21] Y. H. Won, H. S. Jang, K. W. Cho, Y. S. Song, D. Y. Leon, H. K. Kwon, *Opt. Lett.* **2009**, *34*, 1.
[22] R. J. Anthony, D. J. Rowe, M. Stein, J. H. Yang, U. Kortshagen, *Adv. Funct. Mater.* **2011**, *21*, 4042.
[23] A. Gupta, M. T. Swihart, H. Wiggers, *Adv. Funct. Mater.* **2009**, *19*, 696.
[24] E. J. Henderson, A. J. Shuhendler, P. Prasad, V. Baumann, F. Maier-Flaig, D. O. Faulkner, U. Lemmer, X. Y. Wu, G. A. Ozin, *Small* **2011**, *7*, 2507.
[25] C. M. Hessel, E. J. Henderson, J. G. C. Veinot, *Chem. Mater.* **2006**, *18*, 6139.
[26] C. M. Hessel, M. R. Rasch, J. L. Hueso, B. W. Goodfellow, V. A. Akhavan, P. Puvanakrishnan, J. W. Tunnel, B. A. Korgel, *Small* **2010**, *6*, 2026.
[27] N. Shirahata, T. Hasegawa, Y. Sakka, T. Tsuruoka, *Small* **2010**, *6*, 915.
[28] X. Zhang, M. Brynda, R. D. Britt, E. C. Carroll, D. S. Larsen, A. Y. Louie, S. M. Kauzlarich, *J. Am. Chem. Soc.* **2007**, *129*, 10668.
[29] D. P. Puzzo, E. J. Henderson, M. G. Helander, Z. B. Wang, G. A. Ozin, Z. H. Lu, *Nano Lett.* **2011**, *11*, 1585.
[30] F. Maier-Flaig, J. Rinck, M. Stephan, T. Bocksrocker, M. Bruns, C. Kubel, A. K. Powell, G. A. Ozin, U. Lemmer, *Nano Lett.* **2013**, *13*, 475.
[31] M. L. Mastronardi, E. J. Henderson, D. P. Puzzo, Y. L. Chang, Z. B. Wang, M. G. Helander, J. H. Jeong, N. P. Kherani, Z. H. Lu, G. A. Ozin, *Small* **2012**, *8*, 3647.
[32] D. Jurbergs, E. Rogojina, L. Mangolini, U. Kortshagen, *Appl. Phys. Lett.* **2006**, 88.
[33] M. L. Mastronardi, F. Hennrich, E. J. Henderson, F. Maier-Flaig, C. Blum, J. Reichenbach, U. Lemmer, C. Kubel, D. Wang, M. M. Kappes, G. A. Ozin, *J. Am. Chem. Soc.* **2011**, *133*, 11928.
[34] E. J. Henderson, J. A. Kelly, J. G. C. Veinot, *Chem. Mater.* **2009**, *21*, 5426.
[35] N. Shirahata, *Phys. Chem. Chem. Phys.* **2011**, *13*, 7284.
[36] N. Shirahata, D. Hirakawa, Y. Masuda, Y. Sakka, *Langmuir* **2013**, *29*, 7401.
[37] N. Shirahata, M. R. Linford, S. Furumi, L. Pei, Y. Sakka, R. J. Gates, M. C. Asplund, *Chem. Commun.* **2009**, 4684.
[38] C. S. Yang, R. A. Bley, S. M. Kauzlarich, H. W. H. Lee, G. R. Delgado, *J. Am. Chem. Soc.* **1999**, *121*, 5191.
[39] I. N. Germanenko, S. T. Li, M. S. El-Shall, *J. Phys. Chem. B* **2001**, *105*, 59.
[40] X. D. Pi, R. W. Liptak, J. D. Nowak, N. Pwells, C. B. Carter, S. A. Campbell, U. Kortshagen, *Nanotechnology* **2008**, 19.

[41] H. Sugimoto, M. Fujii, K. Imakita, S. Hayashi, K. Akamatsu, *J. Phys. Chem. C* **2013**, *117*, 11850.
[42] B. Ghosh, N. Shirahata, *Sci. Technol. Adv. Mater.* **2014**, *15*, 014207.
[43] M. A. Lampert, *Phys. Rev.* **1956**, *103*, 1648.
[44] D. S. Ginger, N. C. Greenham, *J. Appl. Phys.* **2000**, *87*, 1361.
[45] R. A. M. Hikmet, D. V. Talapin, H. Weller, *J. Appl. Phys.* **2003**, *93*, 3509.
[46] P. O. Anikeeva, C. F. Madigan, J. E. Halpert, M. G. Bawendi, V. Bulovic, *Phys. Rev. B* **2008**, 78. 085434.
[47] B. Kumar, R. Hue, W. L. Gladfelter, S. A. Campbell, *J. Appl. Phys.* **2012**, *112*. 034501.
[48] C. F. Huebner, R. D. Roeder, S. H. Foulger, *Adv. Funct. Mater.* **2009**, *19*, 3604.
[49] L. Qian, Y. Zheng, J. G. Xue, P. H. Holloway, *Nat. Photonics* **2011**, *5*, 543.
[50] W. K. Bae, Y.-S. Park, J. Lim, D. Lee, L. A. Padilha, H. McDaniel, I. Robel, C. Lee, J. M. Pietryga, V. I. Kilmov, *Nat. Commun.* **2013**, *4*, 3661.
[51] D. Bozyigit, V. Wood, *MRS Bull.* **2013**, *38*, 731.
[52] S. Bhattacharjee, I. Rietjens, M. P. Singh, T. M. Atkins, T. K. Purkait, Z. J. Xu, S. Regli, A. Shukaliak, R. J. Clark, B. S. Mitchell, G. M. Alink, A. T. M. Marcelis, M. J. Fink, J. G. C. Veinot, S. M. Kauzlarich, H. Zuilhof, *Nanoscale* **2013**, *5*, 4870.
[53] L. Ruizendaal, S. Bhattacharjee, K. Pournazari, M. Rosso-Vasic, L. H. J. de Haan, G. M. Alink, A. T. M. Marcelis, H. Zuilhof, *Nanotoxicology* **2009**, *3*, 339.